Growth, Structural, and Optical Properties of Self-Assembled (In,Ga)As Quantum Posts on GaAs

9 **AUTHORS**, INCLUDING:

Hubert J Krenner
Universität Augsburg
79 PUBLICATIONS   **1,081** CITATIONS

Craig Pryor
University of Iowa
107 PUBLICATIONS   **2,463** CITATIONS

Jinping Zhang
Chinese Academy of Sciences
47 PUBLICATIONS   **864** CITATIONS

Pierre Petroff
University of California, Santa Barbara
663 PUBLICATIONS   **32,371** CITATIONS

Growth, Structural, and Optical Properties of Self-Assembled (In,Ga)As Quantum Posts on GaAs

J. He,[†] H. J. Krenner,[†] C. Pryor,[‡] J. P. Zhang,[†] Y. Wu,[†] D. G. Allen,[§] C. M. Morris,[§] M. S. Sherwin,[§] and P. M. Petroff*,[†,‖]

Materials Department, University of California, Santa Barbara, California 93106, Department of Physics and Astronomy, University of Iowa, Iowa City, Iowa 52242, Department of Physics, University of California, Santa Barbara, California 93106, and Department of Electrical & Computer Engineering, University of California, Santa Barbara, California 93106

ABSTRACT

Self-assembled quantum dots embedded in semiconductor heterostructures have proved to be a rich system for exploring the physics of three dimensionally confined charges and excitons. We present here a novel structure, which allows adjusting the level of confinement between 3D and 2D for electrons and holes, respectively. The quantum post consists of a quantum dot connected to a short quantum wire. The molecular beam epitaxy deposition of these self-assembled structures is discussed, and their structural and chemical compositions are presented. Their optical properties measured by photoluminescence are compared to an eight-band strain-dependent k.p model incorporating detailed structure and alloy composition. The calculations show electron delocalization in the quantum wire part of the quantum post and hole localization in the strain-induced regions at the ends of the quantum post. The quantum post offers the possibility of controlling the dipole moment in the structure and opens up new means for tuning the intra-subband transitions by controlling its dimensions.

Self-assembled quantum dots have been extensively studied and a good understanding of their electronic and optical properties has been achieved both experimentally[1,2] and theoretically.[3,4] Their quantum confinement properties have been exploited for device applications such as quantum dot lasers,[2] quantum well infrared detectors,[5] single photon quantum dot sources,[6] and ultra-low-threshold quantum dot lasers.[7] On the other hand, until recently, two-dimensional (2D) confined nanowires have been difficult to fabricate and consequently their physical properties and applications have remained relatively unexplored. The recent synthesis of high-quality semiconductor nanorods using the VLS technique has triggered a renewed interest in the fabrication of nanostructures, which integrate quantum dots, quantum wires, and p−n junctions.[8,9] One of the major problems with the nanorod and nanowire structures has been their positioning and contacting to electrodes. The influence of surface traps on the optical and transport properties of nanorods has been partially solved by passivating the surface or using a higher band gap shell layer around the nanorod.[10] Here we demonstrate a novel approach based on the self-assembling of quantum posts (QPs) embedded within an MBE grown heterostructure. The QP is a short quantum wire connected to a seed quantum dot (QD). We demonstrate an effective route for the creation of height-controlled (In,Ga)As QPs on GaAs. Since the QP is self-assembled and embedded into a heterostructure, it is free of surface traps. In this Letter we investigate the composition and structure of self-assembled QPs. The detailed information was then used to model the structures using an eight-band k.p theory, and the results are compared to photoluminescence measurements.

The samples were grown by solid source MBE on semi-insulating GaAs (100) substrates. After the native oxide desorption at 610 °C (pyrometer measured temperature), a buffer layer made of a short-period GaAs/AlAs superlattice followed by 1500 Å GaAs was grown at a substrate temperature of 610 °C. The temperature was then lowered to 530 °C to deposit 2 monolayers (MLs) of InAs with a growth rate of 0.0015 nm/s. This first growth forms the seed QD layer. The QP deposition was carried out using the seed QDs as nucleation centers. A deposition sequence consisting of 7 GaAs MLs followed by 1 ML of InAs was used. A 60 s growth interruption was applied after each GaAs or InAs

* Corresponding author. E-mail: petroff@engineering.ucsb.edu.
† Materials Department, University of California.
‡ Department of Physics and Astronomy, University of Iowa.
§ Department of Physics, University of California.
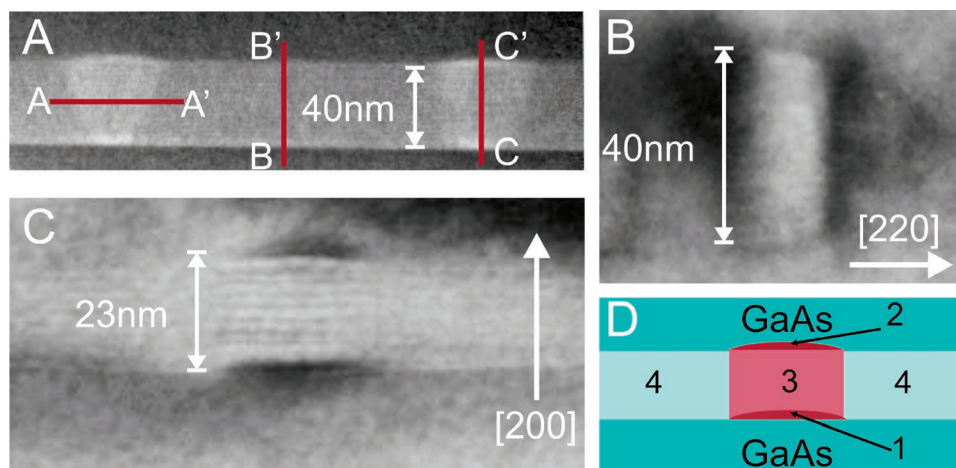‖ Department of Electrical & Computer Engineering, University of California.

Figure 1. Cross sectional images of quantum posts observed in TEM and STEM: (A) Z-contrast image from a high-angle annular dark-field detector in STEM imaging mode, the In rich regions show as bright areas; B and C are conventional contrast TEM images of a 40 nm high and a 23 nm high quantum post with the diffracted beams corresponding to $\mathbf{g} = 220$ and 200, respectively. Chemical analyses with an electron beam scan through the lines illustrated in A are shown in Figure 2.

deposition. Two samples were grown. In the first one, the 7 MLs/1 ML sequence was repeated 8 times, while in the second, the 7 MLs/1 ML sequence was repeated 16 times. The growth rate for GaAs was 0.18 nm/s. During growth, the QD evolution was monitored by reflection high-energy electron diffraction (RHEED). The structural and optical properties of the QPs were investigated by cross sectional transmission electron microscopy (X-TEM), scanning transmission electron microscopy (STEM), and photoluminescence (PL) spectroscopy.

QP samples with a density of approximately 1.5×10^{10} cm^{-2} and a height of 23 and 40 nm, respectively, were prepared for cross-sectional transmission electron microscopy (TEM) analysis and STEM using mechanical polishing and ion and plasma cleaning. Bright field and dark field electron micrographs were taken under two-beam dynamical diffraction conditions ([220] and [400] diffractions conditions) to reveal the strain contrast. Weak beam dark field contrast images ([200] diffraction conditions), which are more sensitive to the chemical composition of the sample, were also taken.

Figure 1A shows a Z-contrast STEM picture of the cross section through two QPs. The Z-contrast imaging is sensitive to composition and weakly dependent on sample thickness variations. The indium-rich areas appear as brighter regions in Figure 1A. In the bright field [220] cross-sectional TEM picture through a 40 nm high QP, the strain contrast at the edges of the QP shows up as dark regions. In Figure 1C a dark field [200] cross-sectional TEM micrograph through a 23 nm high QP is shown. This diffraction condition reveals both chemical and strain contrast in the structure. A schematic of the structure as deduced from the TEM, STEM, and luminescence characteristics is also shown in Figure 1D. The growth direction of the QPs is along the [200] direction.

The QP has a well-defined height set by the deposition conditions and a diameter in the 40 nm range. The shape of the QP is anisotropic and is dependent on the direction of easy In diffusion on the surface. From atomic force microscopy (AFM) and surface studies this direction is known to

be a $[2\bar{2}0]$ direction. This effect can explain the observed difference in the QP shapes observed in parts A−C of Figure 1. The strain contrast and chemical contrast TEM images indicate that the QP is terminated at both ends by QDs (indicated by 1 and 2 in Figure 1D). Region 4 (Figure 1D) contains a short period superlattice with the periodicity of 7 MLs of GaAs and 1 ML of InAs corresponding to the deposition cycle. The weak periodic contrast modulation seen in the Z contrast STEM picture (Figure 1A) shows a period of 22.6 Å, which is consistent with the deposition cycle.

From TEM analysis, we find the self-assembled QP structures to be dislocation-free and coherently strained to the GaAs matrix. The composition of the QP structure has been probed by energy dispersive X-ray (EDX) analysis. The electron beam probe diameter is ≈0.5 nm. The scanned EDX signal is acquired with a low-temperature X-ray fluorescence detector with a resolution of 0.8 nm. The scanned probe signal corresponding to the In EDX signal is shown in Figure 2 for the three scanned directions indicated in Figure 1A.

Figure 2 contains EDX scan profiles for indium as a function of position. The STEM electron beam probe position is moved along AA′, BB′, and CC′ as indicated in Figure 1A. The In distribution along the growth direction in line scans BB′ and CC′ shows the expected sharp composition change as the probe moves from the GaAs cladding layer into layer 3 or 4. On the other hand the line scan along AA′ shows a more noisy signal and smoother In gradient as the electron beam probe is moved from regions 4 to 3 to 4. This probably reflects a gradient in the In segregation in the QP region. The spatial resolution for the chemical analysis is ∼1 nm, and the error in the chemical composition determination is ∼10%.

To quantify the EDX signal and find the composition of the various regions, a $Ga_{0.75}In_{0.15}As$ reference quantum wire with a thickness of 20 nm was grown in each sample to calibrate the Ga and In EDX emission. By comparison with the reference sample, we find a composition of $Ga_{0.9}In_{0.1}As$ for region 4. The QP average composition is found to be $Ga_{0.57}In_{0.43}As$. These compositions are consistent with the

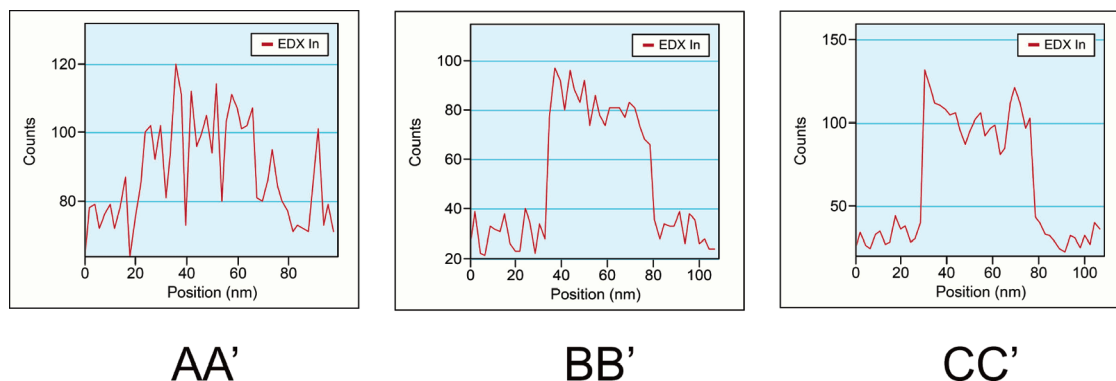AA'   BB'   CC'

Figure 2. Indium composition profiles measured by energy-dispersive X-ray analysis with a 0.5 nm diameter scanning electron probe. The indium profiles are taken along the lines of AA′, BB′, and CC′ shown in Figure 1A.

computed values based on the known amount (12.5%) of In deposited per GaAs (7 MLs)/InAs (1 ML) cycle. If we assume that part of this In diffuses to the high strain regions of the surface and forms the QPs, we can compute the amount of In in the QPs from the measured QD density measured by AFM. For a 10% indium content in the quantum wire matrix (region 4 in Figure 1D), we find a 45% In content in the QPs.

The formation of the QPs proceeds by In transport both along the growth axis and laterally during the extended growth interruptions, which are applied between the GaAs (7 ML) and InAs (1 ML) deposition cycles. Observation of the RHEED pattern shows the characteristic chevrons along the [0$\bar{1}$1] direction after growth of the InAs seed QDs. During deposition of the 7 ML GaAs layers and the following growth interruptions, the chevrons evolve into short, streaky diffraction rods. When the subsequent 1 ML InAs layer is deposited, the RHEED pattern changes back to clear chevrons during the following growth interruption. During the QP buildup,[11] the critical "wetting layer" thickness for InAs QD nucleation, ~1 ML, is much less than the usual 1.7 MLs required for the formation of the InAs seed. A similar effect has been observed in the growth of self-assembled stacked QDs.[12] The indium is known to float on the growth surface when 3−4 MLs of GaAs are deposited on top of InAs.[13] This surface exchange reaction between the Ga and the In contributes to a buildup of film strain energy. This could explain the reduction of the critical wetting layer thickness before In migrates to the regions of highest strain on the surface, i.e., the seed QDs.

Photoluminescence spectra of the QPs were acquired with the samples mounted in a liquid He flow cryostat with a base temperature of $T = 7$ K. Carriers were photogenerated using a titanium:sapphire laser tuned to 800 nm which was focused on the sample to a spot size of ~1 μm. The QP emission was dispersed by a 0.19 mm single grating spectrometer and detected by a liquid N_2 cooled charged coupled device (CCD) detector with a spectral resolution <0.5 meV.

Figure 3 shows the PL spectra taken from QP ensembles with heights of 23 and 40 nm and for different excitation densities. The density for the 23 nm QPs is ~1 × 10^{10} cm^{-2} and the excitation density is increased from $P_0 \approx 0.5$ W·cm^{-2}
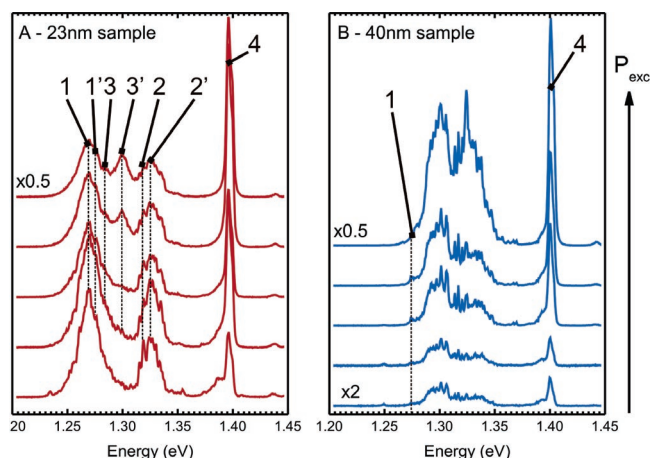

Figure 3. PL spectra of an ensemble of quantum posts for different excitation power: (A) 23 nm QPs; (B) 40 nm QPs. The quantum post density is ~1 × 10^{10} cm^{-2}. The pump power is $P_0 = 0.5$ W·cm^{-2} and $T = 7$ K.

to $P_0 \approx 50$ W·cm^{-2} from the lower to the upper spectrum. For both samples a strong emission peak (line 4) is observed at 1.395 and 1.4 eV, respectively. This signal originates from recombination in the InGaAs short period superlattice (7 MLs of GaAs/1 ML of InAs) matrix surrounding the QPs (region 4, Figure 1D) and is therefore observed for both samples at the same energy and is in good agreement with the bulk band gap of In$_{0.1}$Ga$_{0.9}$As. The PL signal of the 23 nm sample (Figure 3A) shows emission peaks at 1.269, 1.277, 1.315, and 1.325 eV labeled as lines 1, 1′, 2, and 2′, respectively. As the excitation power is increased, line 3 at 1.283 eV and 3′ at 1.299 eV appear. These two lines are blue-shifted by ≈14 and 30 meV from line 1, respectively. This kind of behavior is not observed for conventional QD nanostructures for which states are always filled from lower to higher energies as the pump intensity is increased. The PL signal for the 40 nm QPs shows some marked differences from that of the 23 nm QPs. There is still a low-energy line (line 1) in Figure 3B at 1.275 eV. In addition with increasing pump power, a large number of closely spaced lines appear in the energy range 1.29−1.34 eV.

To obtain further insight into the electronic structure, we performed temperature-dependent PL at a low excitation power density of 1 W·cm^{-2}. Figure 4A shows a false color
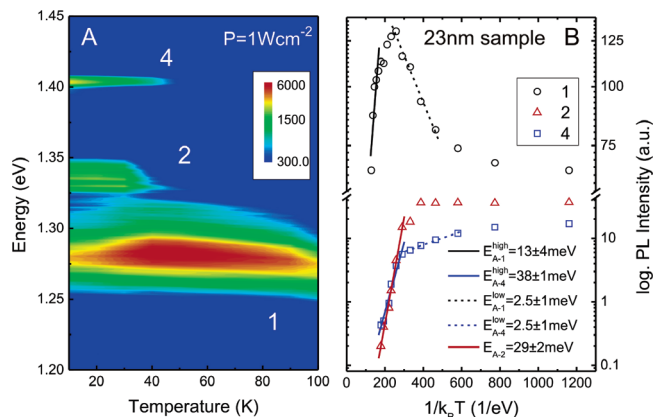
Figure 4. (A) Temperature dependence of the luminescence for the 23 nm QPs. The integrated intensities for lines 1, 2, and 4 shown in Figure 3A are plotted on a color scale with the red as maximum and blue as a minimum. (B) The integrated intensity of the lines as a function of $1/T$ is used to extract the activation energies for lines 1, 2, and 4.

plot of 23 nm QP PL as a function of sample temperature varying from $T = 10$ to 100 K. While peaks 2 and 4 show a clear quenching behavior when the temperature is increased to $T \approx 40$ K, peak 1 continuously gains intensity. Such behavior is different from conventional self-assembled QD structures and suggests a thermally activated transfer of carriers into the lowest lying QP state (peak 1). In order to clarify the various recombination paths, we plot the logarithmic integrated peak intensities of peaks 1, 2, and 4 as a function of $1/k_BT$. For high temperatures (small $1/k_BT$) all signals decrease linearly on this plot with corresponding activation energies of 13 ± 4, 38 ± 1, and 29 ± 2 meV, respectively. Remarkably, in the temperature range between 25 and 60 K, lines 1 and 4 show anticorrelated behavior and exhibit the same slope (2.5 ± 1 meV) with the intensity of line 1 (line 4) increasing (decreasing) by a factor of 2. In contrast, the intensity of line 2′ remains unaffected and almost

constant in this temperature range. The observed anticorrelation between 1 and 4 could result from an increase in carrier transfer from the matrix (region 4, Figure 1D) into the QP (region 1, Figure 1D). The temperature range at which this process occurs suggests that the underlying mechanism could be the thermal breakup of excitons into individual carriers which are captured more efficiently by the QP. Therefore, the surrounding matrix with its lower band gap compared to the GaAs layers above and below the QP layer could act as an intrinsic collection region for carriers, which are then efficiently transferred in the QP.

To understand the PL spectra, we calculated electron and hole energies using an eight-band strain-dependent k.p model[14] using the detailed structural and composition information obtained from the TEM and EDX. Each region of the structure was treated as a uniform alloy with the composition determined from EDX and the corresponding material parameters taken from ref 15, including available bowing parameters. The uniform alloy approximation should be good even if the QP consists of coupled QDs since the barriers between dots would be <1 nm, which is small enough that there should be little change in the effective mass.[16]

Figure 5A shows the computed band diagram and energy levels for electrons and holes along the transverse and growth axis for a 23 nm high QP as well as with the wave function probability densities (Figure 5B). A comparison of the computed model with the PL spectra indicates the following characteristics:

(a) The computed ground state of the QP is approximately 40 meV below the experimentally observed line 1 (Figure 3A) which is within the range expected due to the uncertainties in geometry, composition, and material parameters. With an In concentration of 30% and a diameter of 27 nm, the computed recombination energy is in exact agreement with the measured value. Similarly, a 10% deviation in the
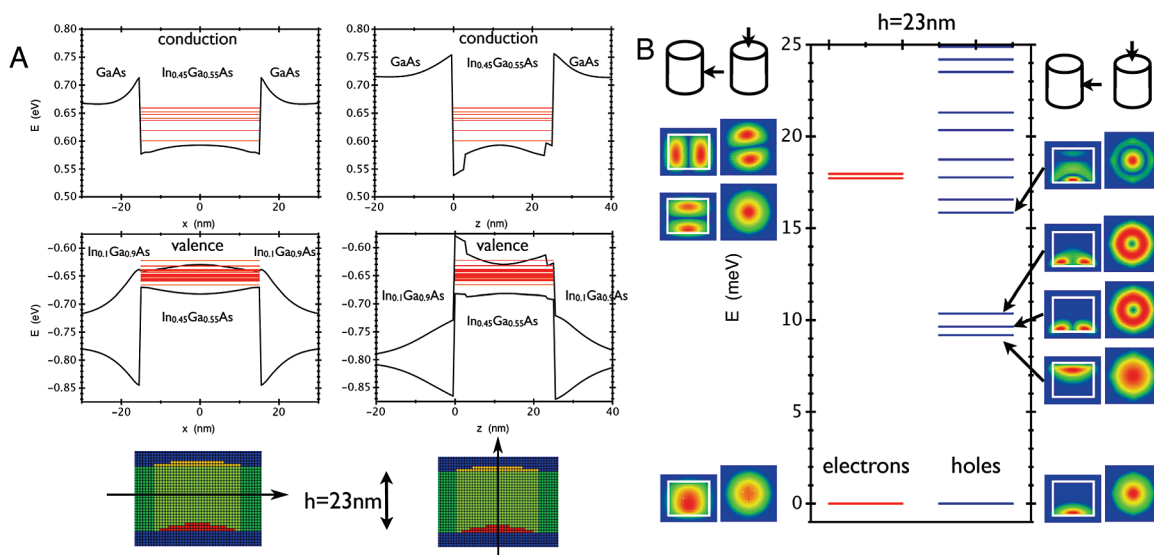

Figure 5. (A) Computed band diagrams and energy levels of electrons and holes (red lines) for the directions indicated on the figure. (B) Computed wave function probability densities and electron and hole energy levels for a 23 nm QP for the two directions indicated in the figure.

hydrostatic deformation potential shifts the QP recombination energy by ~30 meV, similar to single QDs.[17] The small confinement energy makes the QP recombination energy insensitive to the mass parameters. We attribute line 1′ at 1.277 eV, which is blue-shifted by 8 meV from the ground state, to the recombination of the ground state electron with a hole in the first excited-state which is 8−10 meV higher, and localized at the top of the QP.

(b) Line 2′ at 1.325 eV does not correspond to exciton recombination from the top QD (region 2 Figure 1D) but more probably to the recombination of a bound exciton state comprising an electron trapped at the edge of the QD in the matrix and a hole localized in the seed QD. We have estimated the binding energies for excitons free in the QP layer, and with a hole bound in the QP. On the basis of the different reduced masses and including strain-induced mass shifts, we expect $E_{bound} \approx 1.3 E_{free}$, which is in agreement with that obtained from the temperature dependence of the PL spectra (Figure 4).

(c) Lines 3 and 3′ which are found to be blue-shifted by 14 and 30 meV from line 1 at 1.269 eV could match the computed lines which are observed at ≈18 meV (electron first excited-state and hole ground state) and ≈28 meV (electron first excited-state to hole first excited state). The higher energy line 2 observed at 1.315 eV and blue-shifted by 46 meV from line 1 could correspond to the recombination of electrons in the higher excited state (18 meV above the ground state) with the lowest energy hole states (24 meV below the ground hole sate) in Figure 5B.

(d) Finally the computed delocalization of the electron wave along the QP and the localization of the hole state to the seed QD (region 1 in Figure 1D) ensures a very large dipole moment for the QP structure and relaxes the selection rules for the possible recombination processes. The presented tentative attribution shows that the relative energy splitting computed for a model QP structure can be identified in the PL spectra.

The main difference between the 23 and 40 nm sample lies in the intensity and energies of the QP lines. As the length of the QP is increased, the associated emission broadens and the well resolved peak structure of the 23 nm sample is no longer observed. For the 23 nm sample the height of the post is similar to the lateral dimension and, therefore, the associated vertical confinement comparable to the in-plane confinement giving rise to a quasi-zero-dimensional structure. As the QPs′ height is increased to 40 nm, the level spacing corresponding to the longitudinal confinement decreases leading to smearing and broadening of lines. In addition, the absolute energies of these states shift down closer to confined states of the lower QD, giving rise to emission spectrally close to the seed QDs as observed in different QD systems.[18] The computed energy level spectrum for the 40 nm QP (not shown) also indicates a complete delocalization of the electrons while the hole remains strongly localized in the bottom or top quantum dots.

The QP structures are self-assembled and easily integrated into any MBE grown heterostructures and as such are more amenable to efficient electrical carrier injection and band gap engineering. The QP structural connection to QD opens new opportunities for novel devices. For example the combination of quantum wire and quantum dot density of state makes the QPs an attractive structure for low threshold QD lasers. The large dipole moment associated with the localized hole and delocalized electrons makes the QP a very attractive structure for reaching the strong coupling regime in coupled QP-cavity devices. Techniques for self-ordering and positioning[2,19] QPs are easily derived from those used for self-assembled QDs since each QPs is started from a seed self-assembled QD for which self-ordering techniques have been previously demonstrated. Furthermore, QPs can provide self-aligned interconnecting wire between self-assembled QDs. Finally, the QP's growth should be accessible to the wide variety of materials systems for which QDs have been demonstrated (III−V and group IV QDs systems) since their synthesis relies on a growth mode only slightly different from that of the self-assembled QDs.

References

(1) Hogele, A.; Seidl, S.; Kroner, M.; Karrai, K.; Warburton, R. J.; Gerardot, B. D.; Petroff, P. M. *Phys. Rev. Lett.* **2004**, *93*, 21740.
(2) Michler, P. *Single Quantum dots: Fundamentals, Applications and New concepts*; Springer: Berlin, 2003.
(3) Stier, O.; Grundmann, M.; Bimberg, D. *Phys. Rev. B* **1999**, *59*, 5688.
(4) Pryor, C.; Flatte, M. *Phys. Rev. Lett.* **2003**, *91*, 27901.
(5) Tang, S. F.; Chiang, C. D.; Weng, P. K.; Gau, Y. T.; Luo, J. J.; Yang, S. T.; Shih, C. C; Lin S. Y.; Lee, S. C. *IEEE Photonics Technol. Lett.* **2006**, *18*, 986.
(6) Regelman, D. V.; Mizrahi, U.; Gershoni, D.; Erenfreund, E.; Schoenfeld, W.; Petroff, P. M. *Phys. Rev. Lett.* **2001**, *87*, 257401.
(7) Strauf, S.; Hennessy, K.; Rakher, M. T.; Choi, Y. S.; Badolato, A.; Andreani, L. C.; Hu, E. L.; Petroff, P. M.; Bouwmeester, D. *Phys. Rev. Lett.* **2006**, *96*, 127404.
(8) Nilsson, H. A.; Thelander, C.; Froberg, L.; Wagner, J. B.; Samuelson, L. *Appl. Phys. Lett.* **2006**, *89*, 163101.
(9) Bjork, M. T.; Ohlson, B. J.; Sass, T.; Persson, A. I.; Thelander, C.; Magnusson, M. H.; Deppert, K.; Wallenberg, L.; Samuelson, L. *Appl. Phys Lett.* **2002**, *80*, 1058.
(10) Skold, N.; Karlsson, L. S.; Larsson, M. W.; Pistol, M. E.; Selfert, W.; Tragardh, J.; Samuelson, L. *Nano Lett.* **2005**, *5*, 1943.
(11) He, J.; Notzel, R.; Offermans, P.; Koenrad, P. M.; Gong, Q.; Hamhuis, G. J.; Eijkemans, T. J.; Wolter, J. H. *Appl. Phys. Lett.* **2004**, *85*, 2771.
(12) Gerardot, B. D.; Subramanian, G.; Minvielle, S.; Lee, H.; Johnson, J. A.; Schoenfeld, W. V.; Pine, D.; Speck, J. S.; Petroff, P. M. *J. Cryst. Growth* **2002**, *236*, 647.
(13) Silveira, J. P.; Garcia, J. M.; Briones, F. *Appl. Surf. Sci.* **2002**, *188*, 75.
(14) Pryor, C. *Phys. Rev. B* **1998**, *57*, 7190.
(15) Vurgaftman, I.; Meyer, J. R.; Ram-Mohan, L. R.; *J. Appl. Phys.* **2001**, *89*, 5815.
(16) Pryor, C. *Phys. Rev. Lett.* **1998**, *80*, 3579.
(17) Pryor, C. *Phys. Rev. B* **1999**, *60*, 2869.
(18) Schedelbeck, G.; Wegscheider, W.; Bichler, M.; Abstreiter, G. *Science* **1997**, *278*, 1792.
(19) Lee, H.; Johnson, J. A.; He, M. Y.; Speck, J. S.; Petroff, P. M. *Appl. Phys. Lett.* **2001**, *78*, 105.

NL070132R